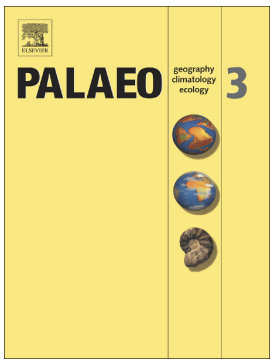

Framboidal pyrite evidence for persistent low oxygen levels in shallow-marine facies of the Nanpanjiang Basin during the Permian-Triassic transition

Yifan Xiao, Kui Wu, Li Tian, Michael J. Benton, Yong Du, Hao Yang, Jinnan Tong

PII: S0031-0182(18)30223-2
DOI: doi:10.1016/j.palaeo.2018.08.012
Reference: PALAEO 8898

To appear in: *Palaeogeography, Palaeoclimatology, Palaeoecology*

Received date: 9 March 2018
Revised date: 21 August 2018
Accepted date: 21 August 2018

Please cite this article as: Yifan Xiao, Kui Wu, Li Tian, Michael J. Benton, Yong Du, Hao Yang, Jinnan Tong , Framboidal pyrite evidence for persistent low oxygen levels in shallow-marine facies of the Nanpanjiang Basin during the Permian-Triassic transition. Palaeo (2018), doi:10.1016/j.palaeo.2018.08.012

Framboidal pyrite evidence for persistent low oxygen levels in shallow-marine facies of the Nanpanjiang Basin during the Permian-Triassic transition

Yifan Xiao[a,b], Kui Wu[a], Li Tian[a,b *], Michael J. Benton[b], Yong Du[a], Hao Yang[a], Jinnan Tong[a*]

[a] *State Key Laboratory of Biogeology and Environmental Geology, School of Earth Science, China University of Geosciences, Wuhan, 430074, China*

[b] *School of Earth Sciences, University of Bristol, BS8 1RJ, UK*

*Corresponding authors: tianlibgeg@163.com (L. Tian); jntong@cug.edu.cn (J. Tong)

Abstract

Previous studies suggested that anoxia was a causal factor in the end-Permian mass extinction (EPME), marked by abrupt enrichment of pyrite framboids in the post-EPME microbialites of the earliest Triassic on shallow platforms, and that this dysoxic–anoxic phase followed a time of well-oxygenated seafloors. Here, we report persistent dysoxia throughout the latest Permian and euxinia just before the EPME, based on a new redox history reconstruction study using framboidal pyrite size distribution as well as sulfur isotopic compositions of pyrites, from the Taiping section on the Pingguo Platform in the Nanpanjiang Basin in China. Further, we show that the EPME was followed here by rapid oxygenation, not an anoxic incursion. This revised redox history might be an unusual localized phenomenon when compared to other platforms, or it could be solid sedimentary evidence for redox oscillations outside the bioclast-enriched photic zone, which broadens our understanding of terrestrial–marine ecosystem interactions before and during the EPME.

Keywords: sulfur isotope; redox condition; Pingguo Platform; microbialite; mass extinction; palaeo-ocean

1. Introduction

Low oxygen has been seen as one of the most important factors in geohistorical mass extinctions of marine invertebrates for decades (e.g. Hallam and Wignall, 1992; Schubert and Bottjer, 1995; Song et al., 2014). Euxinia is known to have occurred within the photic zone during mass extinctions (including the end-Guadalupian, end-Permian, end-Triassic, and Toarcian events), devastating major habitats of benthic metazoans in shallow seas (e.g. Grice et al., 2005; Meyer and Kump, 2008). Widespread and critical low-oxygen conditions in superanoxic and/or stratified oceans have been identified as a major environmental contributor to the end-Permian mass extinction (EPME), which was the biggest mass extinction of the Phanerozoic (e.g. Wignall and Twitchett, 1996; Knoll et al., 1996; Isozaki, 1997).

Physiological stresses imposed on marine life by the mix of warming, anoxia, and ocean acidification associated with hyperthermal events have been identified as a major cause of extinction selectivity during the EPME: broadly speaking, poorly buffered organisms such as corals, sponges, brachiopods, bryozoans, and crinoids died out, whereas well-buffered taxa such as bivalves, gastropods, cephalopods, and ostracods survived (Knoll et al., 1996, 2007). This is not the whole story, however, as there are exceptions, and a broader model for selectivity has been identified as the ‘double whammy’ of lethally hot surface waters and euxinic bottom waters that defined a restricted habitable refuge zone at mid-water depths (Song et al. 2014). These models can be employed for other hyperthermal events, such as those at the end of the Capitanian, mid-Carnian, end-Triassic, and Toarcian Oceanic Anoxia Events (e.g. Bond and Grasby, 2017). If, as we find here, conditions were dysoxic or euxinic before the crisis and oxygenated after, even in a limited number of basins, then this adds complexity to the classic ocean-atmosphere models.

Numerous redox reconstruction studies of different settings globally suggest that euxinia and dysoxia occurred at the Permian-Triassic (P-Tr) transition, although with regional variations (e.g. Wignall and Twitchett, 2002; Bond et al., 2010; Kaiho et al., 2016). Unlike other areas (such as Australia, Europe and boreal areas), South China was thought to record

an oxygenation event immediately after the EPME, rather than an oxygen decline, especially in deeper settings, indicated by multiple proxies, including pyrite morphology, trace elements and biomarkers (Grice et al., 2005; Bond and Wignall, 2010; He et al., 2013; Wei et al., 2015a; Li et al., 2016; Kaiho et al., 2016). Further, Twitchett et al. (2004) reported earliest Triassic invertebrate faunas from Oman that suggested good oxygenation of bottom waters in that region as well, against a backdrop of nearly universal anoxia in the earliest Triassic elsewhere. However, this scenario is debated for shallow marine platforms within the South China Block: U isotope, framboidal pyrite size distributions and sulfur isotopes all suggest a decline of oxygen across the EPME horizon (Algeo et al., 2007, 2008; Brennecka et al., 2011; Liao et al., 2010, 2017; Wang et al., 2015), whereas redox-sensitive elements suggested that oxygenation occurred during the deposition of the post-EPME microbialites (Loope et al., 2013; Collin et al., 2015).

To settle the controversial redox history of shallow platforms and to develop a more comprehensive understanding of the palaeogeographic impact on redox conditions, we present here a case study of the Taiping section, which was located on the Pingguo Platform in the Nanpanjiang Basin during the P-Tr transition. Framboidal pyrites and sulfur isotopes have been widely used as indicators of euxinia and/or dysoxia in P-Tr redox studies (e.g. Wignall et al., 2005; Nielson and Shen, 2004; Gorjan et al., 2007; Algeo et al., 2008, 2010, 2011; Bond and Wignall, 2010; Liao et al., 2010, 2017; He et al., 2013; Dustira et al., 2013; Tian et al., 2014; Wang et al., 2015; Wei et al., 2015b; Li et al., 2016; Huang et al., 2017). We present the pyrite morphology and size distribution of pyrite framboids as well as sulfur isotope compositions of pyrites here to enable us to reconstruct the redox history of the Pingguo Platform and make wider palaeogeographic correlations.

2. Geological setting and methods

The South China Block was located in the eastern realm of Palaeotethys, around < 30°N latitude, in the Permian (Fig. 1). Since then, it has rotated nearly 90° counterclockwise, and the modern southern part, together with the Nanpanjiang Basin, originally faced the western

margin of Panthalassa (Fig. 1). During the Permian and Triassic, the Nanpanjiang Basin was an embayment on the eastern part of the Yangtze Block (Fig. 1). The basin subsided beside these platforms and was filled with argillaceous deposits and/or siliciclastic turbidites during the Middle to Late Triassic (Enos et al., 2006). Several isolated carbonate platforms, called the Great Bank of Guizhou, Debao, Jinxi, Pingguo, Heshan and Chongzuo, developed rapidly from the late Palaeozoic to the Middle Triassic (Fig. 1).

The Taiping section is located 500 m northeast of Taiping Town, Pingguo County, Guangxi Province (23°30'00"N; 107°31'20"E). It was deposited in the northwestern interior of the Pingguo Platform (Fig. 1B). The P-Tr succession consists of the Upper Permian Heshan Formation and Lower Triassic Majiaoling Formation (Fig. 2A). The Heshan Formation is dominated by medium-bedded bioclastic limestones, while some interbedded siliceous limestone/cherts occur in the lower part. The Lower Triassic Majiaoling Formation is characterized by the occurrence of the Permian-Triassic boundary microbialite (PTBM) in the basal part, and oolitic limestone/dolomite in the upper part. The contact surface of these two formations is a distinct lithological turnover surface: the dark grey PTBM was deposited directly on a light-coloured underlying grey bioclastic limestone with a flat surface (red arrow in Fig. 2B). Note that this is not a stylolitised horizon, based on its flat shape and lack of carbonate dissolution, which differs from a true stylolitised surface, which is an irregular, dark, carbonate dissolved surface (blue arrow in Fig. 2B), located 2 cm above the formation contact surface.

Microfacies analyses generally suggest an open-platform interior facies for the P-Tr transition at Taiping (Lehrmann et al., 2003), except that the lowest 1.5 m of the measured section might have been deposited in a deeper water environment (Tian et al., 2018). The occurrences of small foraminifers and sponge spicules (Fig. 3C) in the lowest 1.5 m of the measured section indicate a relatively deeper basin environment, while the abundant algae and foraminifers in the bioclastic limestone of the uppermost Heshan Formation, indicate an extremely shallow open platform environment within the photic zone at inferred water depths of ~10–30 m (Fig. 3A, 3B; Tian et al., 2018). Samples from the microbialites are described

microscopically as dolomitized wackestone, implying a relatively restricted platform environment (Fig. 4; Tian et al., 2018).

Twenty-eight samples, each weighing > 5 kg, were collected and dissolved with 10 % dilute acetic acid for conodont study. These samples also were drilled to measure carbonate carbon isotopes and pyrite sulfur isotopes. About 150–400 μg of bulk sample powder was placed in a butyl rubber septum sealed vial and reacted with 100% phosphoric acid at 72 °C after flushing with helium. By using a MAT 253 mass-spectrometer coupled directly to a Finnigan Gasbench II interface (Thermo Scientific), $\delta^{13}C$ and $\delta^{18}O$ were measured from the evolved CO_2 gas. Isotopic values are reported as per mille relative to the Vienna Pee Dee belemnite (V-PDB) standard, with analytical precision better than ± 0.1 ‰ for $\delta^{13}C$ and ± 0.1 ‰ for $\delta^{18}O$, based on replicate analyses of two laboratory standards, GBW 04416 and GBW 04417 (same method as in Song et al., 2013). By using the $CrCl_2$ reduction method and precipitatation as Ag_2S in silver nitrate traps (Canfield et al., 1986), S_{pyrite} contents were stoichiometrically calculated from the concentration of pyrite sulfur (FeS_2) that was extracted. Then the Ag_2S precipitates from the $CrCl_2$ reduction were put into a Thermo Fisher Scientific Delta V Plus isotope ratio mass spectrometer coupled with a Flash elemental analyser to measure the $\delta^{34}S_{py}$. The $\delta^{34}S$ values are reported relative to the VCDT standard, with better than ± 0.2 ‰ (1σ) of analytical precision, based on replicate analyses of three standards: IAEA S1 (− 0.3 ‰), IAEA S2 (+ 22.65 ‰), and IAEA S3 (− 32.5‰). As a useful redox indicator in modern sediments, framboidal pyrites have also been used in sedimentary rocks as a robust palaeo-redox indicator: a small mean size (< 6 μm) with narrow distribution range indicates euxinia–anoxia, while larger mean sizes with wide variance indicate dysoxia–oxidation (Wignall and Newton, 1998). Vertically oriented polished thin sections (2 x 2 cm) were made for a subset of 14 samples to scan the pyrite morphology by SEM (Hitachi SU 8010).

All these laboratory measurements and observations were done in the State Key Laboratory of Biogeology and Environmental Geology of the China University of Geosciences (Wuhan).

3. Results

3.1. Biostratigraphic and chemostratigraphic correlations

Five species of *Hindeodus* were recovered from the microbialites of the basal Majiaoling Formation, including *H. parvus*, *praeparvus*, *eurypyge*, *changxingensis* and *inflatus* (Fig. 5). The first appearance of *H. parvus* coincides with the lithological contact surface, indicating that the PTB is located at the base of the microbialites (Fig. 6).

Although no conodonts have been discovered, fusulinids and diverse skeletons are abundant in the bioclastic limestone of the Heshan Formation (Fig. 3). Occurrences of Permian fusulinid taxa, including *Nankinella* spp. and *Reichelina* spp., constrain the age of the top of the Heshan Formation to the latest Permian. Along with the last occurrences of these two fusulinid taxa, most foraminifers disappeared at the top of the Heshan Formation, marking the EPME horizon (Tian et al., 2018).

Values of $\delta^{13}C_{carb}$ range from 1.23 to 3.5 ‰, 2.5 ‰ on average, in the uppermost Heshan Formation, while the lowermost Majiaoling Formation is characterized by lower $\delta^{13}C_{carb}$ values (from -0.6 ‰ to 0.6 ‰, -0.6‰ on average). The carbon isotope curve shows a rapid decrease, from 2.4 ‰ to 0.3 ‰, across the lithological contact surface (Fig. 6; Table S1).

Thus, the microbialites of the basal Majiaoling Formation are earliest Triassic in age, while the bioclastic limestone of the uppermost Heshan Formation is latest Permian. Note that the LPME horizon, PTB location and largest $\delta^{13}C_{carb}$ decrease level, all coincide with the lithological contact surface between the bioclastic limestone of the uppermost Heshan Formation and the microbialites of the Majiaoling Formation.

3.2. Size distribution of pyrite framboids and inferred redox history of the Pingguo Platform during the P-Tr transition

Abundant framboidal pyrites have been found in all these 14 SEM-scanned samples, co-occurring with a few or abundant euhedral pyrite grains (Figs. 6, 7; Table S2). We counted 1285 framboidal pyrites, as individuals or in clusters (Fig. 7), with sizes varying from 1.05

μm to 62.50 μm (Fig. 6; Table S2). The mean sizes are relatively small (4.67–8.47 μm) with smaller standard deviations (1.61–4.23) in the uppermost Heshan Formation than in the Majiaoling Formation (7.43–14.95 μm mean sizes, and standard deviations of 2.54–3.70) (Table S2).

Based on these numerical criteria, ratios of mean size and standard deviation of each sample (Wilkin et al., 1996; Bond and Wignall, 2010) indicate that two of the Taiping samples suggest euxinic conditions, while the other 12 samples show dysoxic conditions (Fig. 8). The samples with relatively large mean sizes or standard deviations (TP-7, TP-10 and TP-11) contain abundant authigenic pyrites, indicating potential dysoxic–oxic redox conditions (Table S2). Further, the framboidal pyrites in sample TP-7 are distinctively influenced by diagenesis, showing overgrown edges (Fig. 7). Since sample TP-7 is a sandy limestone enriched in detrital minerals such as quartz and feldspar, the restored watermass redox condition of this "detrital event" interval might be questionable because of mixing with allochthonous minerals.

In addition, the redox history of the Pingguo platform during the Permian-Triassic transition has been reconstructed by using temporal size variations of these samples (Table S2; Figs. 6, 8, 9): (1) the lower section (0–600 cm in cumulative thickness) contains moderate mean-sized framboidal pyrites with moderate to large standard deviations, indicating dysoxic redox conditions; (2) the uppermost 100 cm of the Heshan Formation contains small mean-sized framboidal pyrites with small standard deviations, suggesting a euxinic watermass; (3) the lowest 90 cm of the Majiaoling Formation contains large mean-sized framboidal pyrites with moderate standard deviations, implying dysoxic–oxic conditions; and (4) the upper measured parts of the Majiaoling Formation contain moderate mean-sized framboidal pyrites with moderate standard deviations, indicating dysoxic redox conditions. Generally speaking, the results suggest that persistent dysoxia occurred in the Taiping section through the P-Tr. Transition, with occasional euxinic incursions in the latest Permian, and potential oxygenation in the immediate aftermath of the EPME in the earliest Triassic.

3.3. Sulfur isotopic compositions of pyrite and the indicated pre-LPME pyrite input

The $\delta^{34}S_{pyrite}$ data of the Heshan Formation show large variations and some positive values from -23.4 ‰ to 4.2 ‰ (Fig. 6 and Table S1). The temporal variation shows relatively stable values from -23.4 ‰ to -11.2 ‰, excluding high values from -3.6 ‰ to 4.2 ‰ in the 450–600 cm interval of the measured section. Otherwise, $\delta^{34}S_{pyrite}$ of the basal Majiaoling microbialite varied from -25.5 ‰ to -10.1 ‰ without any evident trend of temporal variation. Additionally, $\delta^{34}S_{pyrite}$ increased slightly across the EPME, although the framboidal pyrites indicated redox conditions alternated from euxinic to dysoxic–oxic abruptly (see section 3.2). In fact, except for the 450–600 cm interval of the measured section, no significant variation or evident temporal trend occurred in $\delta^{34}S_{pyrite}$ values (Fig. 6).

4. Discussion

4.1 *Pre-EPME euxinia-dysoxia of shallow marine watermass*

Before this study, framboidal pyrites had been reported from several microbialite-bearing P-Tr successions in South China. Liao et al. (2010) first discovered abundant relatively large framboidal pyrites in the microbialites of the Chongyang section on the Yangtze Platform, while framboidal pyrites were rarely found in the underlying pre-EPME bioclastic limestone. The same pattern has also been repeatedly found in the Cili and Dajiang sections (located on the Yangtze Platform and Great Bank of Guizhou, respectively; Wang et al., 2015; Liao et al., 2017). All these studies demonstrate that oxygen in the shallow watermass reduced after the EPME. However, we have not only found abundant framboidal pyrites in the microbialites of the Taiping section, but also in the underlying pre-EPME bioclastic limestone, presenting an exceptional case that differs from previous findings: persistent dysoxia occurred before and after the EPME on the Pingguo Platform rather than a process of gradually declining oxygen. The $\delta^{34}S_{pyrite}$ values also show no significant variations between the uppermost Permian bioclastic limestones (except the samples from the detrital interval) and the lowermost

Triassic microbialites, supporting the suggestion of persistent dysoxia across the EPME at Taiping.

Previously, framboidal pyrites had been found in the latest Permian bioclastic limestone of several shallow carbonate platform settings without the overlying PTBMs, such as in the Bulla section in Italy and the Bálvány North section in Hungary. Bond and Wignall (2010) reported occurrences of framboidal pyrites in the Upper Permian Nagyvisnyó Limestone Formation of the Bálvány North section. However, the small number of framboidal pyrites in the sample ($n < 30$) and relatively large mean size (7.4–11 μm) with large standard deviations (3.5–6) implied dysoxic–oxic redox conditions (Bond and Wignall, 2010). Not only Gorjan et al. (2007), but also Bond and Wignall (2010) reported abundant framboids in the bioclastic limestones and oolites below and above the extinction horizon in the Bulla section, implying that shallow marine dysoxia lasted from pre-EPME to post-EPME. However, in these conditions of strong water energy implied by the oolites, minerals and grains like pyrite, framboids might be transported from the dysoxic–anoxic deep water by upwelling (Kershaw, 2015), so invalidating these framboidal pyrites as reliable evidence for pre-EPME shallow marine euxinia–dysoxia.

Meanwhile, low $\delta^{34}S_{pyrite}$ values (< -20‰) had barely been reported in the pre-EPME bioclastic limestone of other well-studied shallowing marine settings, including the Nhi Tao section (Vietnam) and Bulla section (Italy). As we discussed above, associated with the pre-EPME small abundant framboidal pyrites, the first $\delta^{34}S_{pyrite}$ negative shift in the Bulla section was recorded in oolites, very likely to have been mixed by the strong water energy. Otherwise, $\delta^{34}S_{pyrite}$ values at Taiping coincide with those in the Nhi Tao section (from ~-20 ‰ to ~10 ‰) below the EPME horizons (Fig. 6; Algeo et al., 2008). Based on the model proposed by Algeo et al. (2008), these values could have been caused by mixing of syngenetic with authigenic pyrites, at varying ratios from ~1:1 (resulting in ~-20 ‰ of $\delta^{34}S_{pyrite}$) to fully authigenic (~10 ‰ of $\delta^{34}S_{pyrite}$).

The interval with high $\delta^{34}S_{pyrite}$ (-3.6 ‰ – 4.2 ‰) corresponds to the "foram gap & detrital event" uncovered by Tian et al. (2018), in which abundant detrital minerals were found at the

490–500 cm level of the measured section, indicating rapid terrestrial input. Abundant euhedral pyrites have also been found co-occurring with framboidal pyrites in this interval (Fig. 7E). The observed detrital minerals and euhedral pyrites suggest that strong terrestrial inputs contributed to the high $\delta^{34}S_{pyrite}$ values. The mixing of syngenetic pyrite with authigenic pyrites in shallow marine settings has been modelled by Algeo et al. (2008), and our data generally show higher values than this upwelling-mixed model by $\delta^{34}S_{pyrite}$/Pyrite S (Fig. 9). Nielson and Shen (2004) noted 11.5 ‰ of $\delta^{34}S_{pyrite}$ from the Permian evaporates, providing us with a comparable case to hypothesise a model in which terrestrial/neritic evaporates caused high $\delta^{34}S_{pyrite}$ in shallow seawater. Thus, it should be reasonable to infer that the heavy $\delta^{34}S_{pyrite}$ was transported into the shallow sea by the terrestrial inputs, suggesting a new dynamic for the heavy $\delta^{34}S_{pyrite}$ in marine sediments (Fig. 9).

Thus, our new discovery in the Taiping section is the first reliable report of abundant relatively small framboidal pyrites with low $\delta^{34}S_{pyrite}$ values (-23.4 ‰ to -11.6 ‰) in pre-EPME shallow marine rocks, providing solid evidence of pre-extinction euxinia–dysoxia. The uppermost Permian bioclastic limestones are composed of algal-foraminiferal packstones, except for the sandy limestone bed, indicating a shallow platform without significant reworking activity (Figs. 4, 6). The two samples with small mean-sized pyrite framboids (TP-8 and TP-9), indicating a euxinic water mass, provide solid evidence for shallow marine euxinia before the EPME (Figs. 6, 10). Coeval euxinia with abundant skeletons occurring before the EPME in the Taiping section, as presented in this study, indicates that substantial redox oscillations occurred before the EPME in this shallow marine setting (Fig. 10).

Pre-EPME redox oscillations have been identified in slope and deep-water facies of South China. Ding et al. (2015) recorded numerous anoxic intervals through the Heshan and Dalong formations in South China, based on sedimentary and trace fossil evidence. They noted a peak of anoxia at the Wuchiapingian–Changhsingian boundary in seabed sediments, but assumed the surface waters were oxic. However, abundant evidence from the Dalong Formation, including iron speciation, biomarkers, and framboidal pyrites, suggests episodic Changhsingian euxinia–anoxia, prior to the EPME, in many basinal settings in South China.

The peak of the euxinia–anoxia was found in the early to middle rather than late Changhsingian (e.g. Wei et al., 2015b; Shen et al., 2016; Lei et al., 2017).

Late Permian deep water euxinia–anoxia in the open Panthalassic Ocean has not yet been confirmed. Long-term Late Permian to Middle Triassic anoxia was identified in deep basin successions in Japan and British Columbia by Isozaki (1997). He proposed that there had been a superanoxic ocean episode lasting from the base of the Changhsingian to the Anisian, during which the Panthalassic Ocean was stratified, rather like the Black Sea today, with euxinic deep waters and oxic surface waters containing radiolarians and other plankton. However, the Isozaki model was questioned by Zhang et al. (2001) and others (e.g. Wignall et al., 2010). Data from other sections in Japan confirmed widespread evidence for intense euxinia just above the EPME horizon rather than longer term prior to the EPME (e.g. Wignall et al., 2010; Algeo et al., 2011; Takahashi et al., 2014).

Like the situation of these inner shelf basins on the Yangtze Platform, Late Permian euxinia–anoxia had been reported in other inner shelf/restricted basins. In the Zechstein Sea in Europe, an evaporitic basin with very different water chemistry to South China, geochemical studies have also shown that euxinia developed and periodically impinged on shallow marine carbonate parts of the basin in the Late Permian (Słowakiewicz et al., 2015). However, these authors argue that euxinia did not occur across the whole basin, but was restricted to marginal settings based on the absence or low biomarker indices for euxinia in other facies. Low sulfur isotopes and abundant small-sized framboidal pyrites in the Ravnefjeld Formation indicate episodic euxinia in the East Greenland Basin during the Late Permian (Nielson and Shen, 2004), while enrichment in small framboidal pyrites in the Hovea core from the Perth Basin (western Australia) showed long-term Late Permian euxinia–anoxia in basinal sediments on the margin of Perigondwana (Bond and Wignall, 2010). These results suggest that the basinal water was generally dysoxic in the East Greenland Basin during the Late Permian, with episodic euxinia incursions long before or after the EPME (Bond et al., 2015; Wignall et al., 2016).

Thus, pre-EPME dysoxia might have been extensive in both the open Panthalassa Ocean and inner shelf basins, while euxinia–anoxia has just been recorded in inner shelf basins before the EPME, implying a potential locally-driven euxinia–anoxia mechanism in the Late Permian, rather than intensive worldwide oceanic stagnation, which might not have happened until the aftermath of the EPME.

4.2 *Earliest Triassic oxygenation event*

As an exceptional case compared to previous framboidal studies on PTBMs, our results from Taiping suggest that the PTBM started to be deposited in well-oxygenated conditions in the immediate aftermath of the EPME. The framboidal pyrites we measured in the basal PTBM of the Taiping section (Table S2; Fig. 10) are significantly larger than previous findings in the Laolongdong, Cili and Dajiang sections (Liao et al., 2010; 2017; Wang et al., 2015). Two of the samples (TP-10 and the TP-11) imply a more oxygenated water mass than in the other sections, while the other three samples of the PTBM at Taiping are similar to previous findings, indicating dysoxia (Table S2; Fig. 8). Although Liao et al. (2010, 2017) reported abundant small-sized framboidal pyrites in PTBMs (indicating anoxia; one sample in Laolongdong and six samples in Dajiang), the PTBMs were generally dysoxic, based on the enrichment of large-sized framboidal pyrites in the other PTBM samples (Liao et al., 2017). The sulfur and carbon isotopic compositions in the Nhi Tao section in Vietnam (located in the Nanpanjiang Basin within the South China Block during the P-Tr transition) show that evidence for shallow marine anoxia–euxinia, covariations of low $\delta^{34}S_{pyrite}$ values and negative $\delta^{13}C_{carb}$, were recorded only episodically with a normal oxygen level background in the post-EPME carbonates. No such obvious covariations of sulfur and carbon isotopes have been observed in the post-EPME rocks at Taiping (Fig. 6), providing no evidence for potential anoxic incursions into the shallow marine setting. In the GSSP Meishan section, intensive oxygenation in Bed 27, which might be the lithological and biostratigraphic equivalent to the PTBM (Xie et al., 2010; Zheng et al., 2013; Yin et al., 2014; Tian et al., 2015), was inferred, based on biomarkers, sulfur isotopes, trace fossils, framboidal pyrites and biofabric

compositions (e.g. Grice et al., 2005; Cao et al., 2009; Zhao and Tong, 2010; Chen et al., 2015; Li et al., 2016). Similar results, based on framboidal pyrites, were also noted from deeper facies sections, including Shangsi, Tianqiao, Changtanhe, Xiakou, Chaohu and Xiaojiaba (Fig. 11; Bond and Wignall, 2010; He et al., 2013; Wei et al., 2015b; Shen et al., 2016; Huang et al., 2017).

Bond and Wignall (2010) demonstrated that this oxygenation event in the immediate aftermath of the extinction was extensive in South China, differing from the expanding euxinia–anoxia pattern in other areas (Fig. 11). A hiatus in the latest Permian and earliest Triassic of these PTBM-bearing sections, makes it inappropriate to compare our data with sections in the Boreal Shelf Sea, in which abundant small framboidal pyrites were noted in the Late Permian Kapp Starostin Formation and rare framboids in the basal Vardebukta Formation (Fig. 11; Bond and Wignall, 2010; Dustira et al., 2013). Equally, the previous report of oxygenated conditions in the earliest Triassic from Oman (Twitchett et al., 2004) cannot be compared directly with our data from China because the Oman section begins in the earliest Triassic (Griesbachian), which sits directly on a Guadalupian-aged limestone, and Upper Permian rocks are absent. Twitchett et al. (2004) interpreted the Oman Griesbachian fauna in oxygenated reef limestones as evidence for extremely rapid recovery of life, but these authors were unable to identify whether it had been preceded by an anoxic phase, either Late Permian or earliest Triassic in age, because of the absence of strata of that age.

4.3 *Implications for palaeoceanic circulation*

Documented redox histories of different successions in varied facies, reconstructed by pyrite morphology and size distribution, show regional variations in the latest Permian and earliest Triassic (Fig. 11). The results from the Pingguo Platform might indeed be a local exception to the widespread shift from oxygenated conditions before the EPME crisis to anoxia afterwards, as seen on other platforms (Fig. 11). Taking the isolated platforms in the Nanpangjiang Basin as examples, our results suggest that the Pingguo Platform recorded dysoxia with euxinia before the EPME, followed by an immediate oxygenation and

subsequent dysoxia in the aftermath of the event, while an oxygen reduction process across the EPME was recorded on the Great Bank of Guizhou (GBG) based on the abundances of framboidal pyrites in the PTBM (Algeo et al., 2008; Liao et al., 2017). Meanwhile, Algeo et al. (2007) demonstrated that the first enrichment of pyrite (especially framboidal) coincided with the EPME in the Nhi Tao section, located on the Jinxi Platform, and this conclusion was supported by high sulfur and organic carbon ratios and a negative pyrite sulfur isotope shift, indicating an oxygen reduction redox history on the Jinxi Platform. On a wider scale, the Laolongdong section and Cili section on the northern margin of the Yangtze Platform, recorded a common oxygen reduction process across the EPME, based on the lack of framboidal pyrites in the pre-EPME strata (Liao et al., 2010; Wang et al., 2016).

The measured $\delta^{34}S_{pyrite}$ values in the Taiping section also show different patterns of change from other shallow marine carbonate successions, implying spatial variation in redox-changing patterns in shallow marine settings during the P-Tr transition. Algeo et al. (2008) studied the sulfur isotopes of the Nhi Tao section (Vietnam), discovering over nine pyritic beds with low $\delta^{34}S_{pyrite}$ (mainly < -20 ‰, lowest approximate to -30 ‰) above the EPME horizon. Gorjan et al. (2007) reported two distinct negative shifts of $\delta^{34}S_{pyrite}$ (documented as $\delta^{34}S_{sulfide}$ by Gorjan et al., 2007) in the Bulla section, < -30 ‰, associated with abundant small pyrite framboids, below and above the EPME horizon, respectively. At Taiping, the $\delta^{34}S_{pyrite}$ values show slight perturbations throughout the EPME, exclusive of the potential terrestrial transported heavy $\delta^{34}S_{pyrite}$ in the 450–600 cm interval of the measured section (see section 4.1), suggesting persistent low oxygen levels. In addition, a relatively constant $\delta^{34}S_{pyrite}$ pattern has also been found in several basinal sections, e.g. West Blind Fjord and Ubara (Algeo et al., 2011, 2012), implying complicated oceanic redox correspondences during the P-Tr transition.

The Taiping section was located much closer to the basin centre than the sections on the GBG and Jinxi Platforms (Fig. 1), suggesting that the dysoxia–euxinia incursion before the EPME might have occurred from the centre of the Nanpangjiang Basin. The widely distributed latest Permian basinal successions of South China (including the Nanpanjiang

Basin) are composed of bedded chert, black shale and siliceous mudstone/limestone, collectively named the Dalong Formation. Multiple lines of evidence (high TOC, abundant small framboidal pyrites, and high Fe_{HR}) suggest significant euxinia–dysoxia in the Dalong Formation, not just in the Nanpanjiang Basin, but also in the sub-basins on the northern margin of the Yangtze Platform (He et al., 2013; Wei et al., 2015; Lei et al., 2017). Liao et al. (2017) attempted to explain the relatively smaller framboidal pyrites in the Dajiang section than in the Laolongdong and Cili sections on the Yangtze Platform by the fact that the Nanpangjiang Basin faced Panthalassa at the time, and perhaps deep-oceanic waters might have intruded, bringing anoxia. However, the Jinxi Platform was located more towards the east than the Pingguo Platform, but recorded the same pattern as the GBG (see discussion in last paragraph). Further, as we discussed in section 4.1, euxinia was recorded in the Dalong Formation; otherwise, dysoxia (not euxinia–anoxia) was extensively recorded in the Panthalassa pre-EPME successions, so implying that the pre-EPME anoxia–euxinia incursions might have come from inner shelf basins, rather than Panthalassa as the proposed origin for the post-EPME shallow marine euxinia–anoxia (Liao et al., 2017). In addition, the heavy $\delta^{34}S_{pyrite}$ by terrestrial input, which was just prior to the latest Permian euxinia at Taiping (see section 3.3), also implies a strong intra-shelf influence on the Pingguo Platform, rather than upwelling from the deep abyssopelagic ocean (which should be marked by extremely low $\delta^{34}S_{pyrite}$ values; see Algeo et al., 2008 and Zhang et al., 2017).

The earliest Triassic seafloor oxygenation in South China, of the shallow platform uncovered herein and in deeper facies (Bond and Wignall, 2010; He et al., 2013; Li et al., 2016), could be taken to mean that the ocean anoxia–euxinia models linked to the P-Tr hyperthermal crisis are wrong, or they could simply provide evidence for variability between basins on a regional scale on the edges of worldwide anoxic oceans (Knoll et al. 2007). However, the classic numerical model for oceanic euxinia following huge volcanic activity posits extensive anoxia–euxinia, including shallow-water euxinia, but stable oceanic gyre regions can retain an oxygenated wind-mixed layer (Meyer and Kump, 2008). A more likely explanation is that reduced marine productivity in the South China Block area occurred

following the EPME, providing insufficient C_{org} sinking flux for oceanic anoxia (Algeo et al., 2013).

There are two proposed models for redox oscillations before and during the EPME: (1) the chemocline might have moved upwards episodically by shoalings/upwellings of deep anoxic water associated with thermal crises, introducing dysoxia–euxinia into shallower sediments, based on evidence of framboidal pyrites and sulfur isotopes (e.g. Bond and Wignall, 2010; Kershaw, 2014; Tian et al., 2014; Huang et al., 2017; Zhang et al., 2017); or (2) enhanced terrestrial inputs into the ocean, caused by de-vegetation and the associated climate changes, led to rapid blooms of bacteria moving from onshore to offshore, and increasing productivity associated with strong sulfate reduction, which can contribute to the formation of framboidal pyrites and sulfur isotope anomalies (e.g. Zhou et al., 2016; Kaiho et al., 2016). No matter what caused the shallow-marine euxinia dynamically, the episodically abundant small-sized pyrite framboids in limited shallow carbonate layers, e.g. Nhi Tao section (Algeo et al., 2007, 2008) and Taiping section (this study), suggest that short-term euxinic events are likely to be the mechanism that can reconcile the evidence of euxinia with generally dysoxic–oxic shallow-marine facies, before, during and after the EPME.

New evidence has suggested that the terrestrial crisis might have occurred earlier than the marine crisis and the inputs from de-vegetated lands into the oceans might have significantly impacted the environmental conditions in the ocean before the marine EPME (e.g. Shen et al., 2011; Zhou et al., 2016; Kaiho et al., 2016; Liu et al., 2017; Dudás et al., 2017). Tian et al. (2018) discovered a “Foram gap & detrital event” in the sandy limestone of the Heshan Formation, 230 cm below the EPME horizon, in the latest Permian of the Taiping section, implying strong terrestrial input and supporting the idea of an ecosystem collapse on land. Along with the results proposed in this study, the potential terrestrial impacted environmental devastations occurred prior to the EPME in the shallow marine.

5. Conclusions

Framboidal pyrites from the Taiping section reveal that persistent euxinia–dysoxia occurred on the shallow marine Pingguo Platform during the Permian-Triassic transition. Abundant small-sized framboidal pyrites below the EPME horizon indicate that euxinia occurred before the EPME, whereas an oxygenation event in the immediate aftermath of the EPME is indicated by the enrichment of large-sized framboidal pyrites in the basal beds of the PTBM. Since the inferred redox history of the Pingguo Platform might be an exceptional case, differing from other shallow carbonate platforms, it provides new evidence for exploring the marine redox history during the P-Tr transition.

Acknowledgments

We thank Prof. Zhong-Qiang Chen, Zihu Zhang and Gan Liu for technical assistance in the laboratory measurements. Special acknowledgements are given to Prof. Thomas Algeo for sharing his unpublished data on the Taiping section and providing constructive discussions, as well as helpful comments and edits in the publication process. This study was supported by the National Science Foundation of China (grants nos. 41530104, 41602024 and 41661134047), the State Key Laboratory of Biogeology and Environmental Geology (GBL11605) and the international exchange programme funded by the postgraduate school of CUG (to Y.X.). This is part of a research project funded by the China Postdoctoral Science Foundation (CPSF), and it also benefited from the sponsored international exchange programme to L.T. (by CPSF). Funded also by NERC BETR grant NE/P013724/1 to M.J.B. It is also a contribution to IGCP 630.

References

Algeo, T.J., Ellwood, B., Nguyen, T.K.T., Rowe, H., Maynard, J.B., 2007. The Permian-Triassic boundary at Nhi Tao, Vietnam: Evidence for recurrent influx of sulfidic watermasses to a shallow-marine carbonate platform. Palaeogeography, Palaeoclimatology, Palaeoecology 252, 304–327.

Algeo, T.J., Hinnov, L., Moser, J., Maynard, J.B., Elswick, E., Kuwahara, K., Sano, H., 2010. Changes in productivity and redox conditions in the Panthalassic Ocean during the latest Permian. Geology 38, 187–190.

Algeo, T.J., Kuwahara, K., Sano, H., Bates, S., Lyons, T., Elswick, E., Hinnov, L., Ellwood, B.B., Moser, J., Maynard, J.B., 2011. Spatial variation in sediment fluxes, redox conditions, and productivity in the Permian–Triassic Panthalassic Ocean. Palaeogeography, Palaeoclimatology, Palaeoecology 308, 65–83.

Algeo, T.J., Shen, Y.A., Zhang, T.G., Lyons, T., Bates, S.M., Rowe, H., Nguyen, T.K.T., 2008. Association of ^{34}S-depleted pyrite layers with negative carbonate δ^{13}C excursions at the Permian-Triassic boundary: Evidence for upwelling of sulfidic deep-ocean water masses. Geochemistry, Geophysics, Geosystems 9, e4.

Algeo, T.J., Henderson, C.M., Ellwood, B., Rowe, H., Elswick, E., Bates, S., Lyons,T., Hower, J.C., Smith, C., Maynard, B., Hays, L.E., Summons, R.E., Fulton, J., Freeman, K.H., 2012. Evidence for a diachronous Late Permian marine crisis from the Canadian Arctic region. Geological Society of America Bulletin 124,1424–1448.

Algeo, T.J., Henderson, C.M., Tong, J.N., Feng, Q.L., Yin, H.F., Tyson, R.V., 2013. Plankton and productivity during the Permian-Triassic boundary crisis: an analysis of organic carbon fluxes. Global and Planetary Change 105, 52–67.

Bond, D.P.G., Grasby, S.E., 2017. On the causes of mass extinctions. Palaeogeography, Palaeoclimatology, Palaeoecology 478, 3–29.

Bond, D.P.G., Wignall, P.B., Joachimski, M.M, Sun, Y., Savov, I., Grasby, S.E., Beauchamp, B., Blomeier, D.P.G., 2015. An abrupt extinction in the Middle Permian (Capitanian) of the Boreal Realm (Spitsbergen) and its link to anoxia and acidification. Geological Society of America Bulletin 127, 1411–1421.

Bond, D.P.G., Wignall, P.B., 2010. Pyrite framboid study of marine Permian-Triassic boundary sections: a complex anoxic event and its relationship to contemporaneous mass extinction. Geological Society of America Bulletin 122, 1265–1279.

Brennecka, G.A., Herrmann, A.D., Algeo, T.J., Anbar, A.D., 2011. Rapid expansion of oceanic anoxia immediately before the end–Permian mass extinction. Proceedings of the National Academy of Sciences, U.S.A. 108, 17631–17634.

Burgess, S.D., Bowring, S., Shen, S.Z., 2014. High-precision timeline for Earth's most severe extinction. Proceedings of the National Academy of Sciences, U.S.A. 11, 3316–3321.

Cao, C.Q., Love, G.D., Hays, L.E., Bowring, S.A., Wang, W., Shen, S.Z., Summons, R.E., 2009. Biogeochemical evidence for euxinic oceans and ecological disturbance presaging the end-Permian Mass Extinction Event. Earth and Planetary Science Letters 281, 188–201.

Chen, Z.Q., Yang, H., Luo, M., Benton, M.J., Kaiho, K., Zhao, L., Huang, Y., Zhang, K., Fang, Y., Jiang, H., 2015. Complete biotic and sedimentary records of the Permian-Triassic transition from Meishan section, South China: Ecologically assessing mass extinction and its aftermath. Earth-Science Reviews 149, 67–107.

Collin, P.-Y., Kershaw, S., Tribovillard, N., Crasquin-Soleau, S., 2015. Geochemistry of post-extinctionmicrobialites as a powerful tool to assess the oxygenation of shallow marine water in the immediate aftermath of the end-Permian mass extinction. International Journal of Earth Sciences 104, 1025–1037.

Ding, Y., Cao, C.Q., Zheng, Q.F., 2015. Lopingian (Upper Permian) trace fossils from the northern Penglaitan Section, Laibin, Guangxi, South China and their environmental implications. Palaeoworld 25, 377–387.

Dudás, F.Ö., Yuan, D.X., Shen, S.Z., Bowring, S.A., 2017. A conodont-based revision of the $^{87}Sr/^{86}Sr$ seawater curve across the Permian-Triassic boundary. Palaeogeography, Palaeoclimatology, Palaeoecology 470, 40–53.

Dustira, A.M., Wignall, P.B., Joachimski, M., Blomeier, D., Hartkopt–Fröder, C., Bond, D.P.G., 2013. Gradual onset of anoxia across the Permian–Triassic Boundary in Svalbard, Norway. Palaeogeography, Palaeoclimatology, Palaeoecology 374, 303–313.

Enos, P., Lehrmann, D.J., Wei J.Y., Yu, Y.Y., Xiao, J.F., Chaikin, D.H., Minzoni, M., Berry, A.K., Montgomery, P., 2006. Triassic evolution of the Yangtze Platform in Guizhou

Province, People's Republic of China. Geological Society of America Special Paper 417, 105 pp.

Forel, M.B., Crasquin, S., Kershaw, S., Collin, P.Y., 2013. In the aftermath of the end-Permian extinction: the microbialite refuge? Terra Nova 25, 137–143.

Forel, M.B., Crasquin, S., Kershaw, S., Feng, Q.L., Collin, P.Y., 2009. Ostracods (Crustacea) and water oxygenation in the earliest Triassic of South China: implications for oceanic events at the end-Permian mass extinction. Australian Journal of Earth Sciences 56, 815–823.

Gorjan, P., Kaiho, K., Kakegawa, T., Niitsuma, S., Chen, Z.Q., Kaiiwara, Y., Nicora, A., 2007. Paleoredox, biotic and sulfur-isotopic changes associated with the end-Permian mass extinction in the western Tethys. Chemical Geology 244, 483–492.

Grice, K., Cao, C., Love, G.D., Böttcher, M.E., Twitchett, R.J., Grosjean, E., Summons, R.E., Turgeon, S.C., Dunning, W., Jin, Y., 2005. Photic zone euxinia during the Permian–Triassic superanoxic event. Science 307, 706–709.

He, L., Wang, Y.B., Woods, A., Li, G.S., Yang, H., Liao, W., 2013. An oxygenation event occurred in deep shelf settings immediately after the end-Permian mass extinction in South China. Global and Planetary Change 101, 72–81.

Huang, Y.G., Chen, Z.-Q., Wignall, B.P., Zhao, L.S., 2017. Latest Permian to Middle Triassic redox condition variations in ramp settings, South China: Pyrite framboid evidence. Geological Society of America Bulletin 129, 229–243.

Isozaki, Y., 1997. Permo–Triassic boundary superanoxia and stratified superocean records from lost deep sea. Science 276, 235–238.

Kaiho, K., Saito, R., Ito, K., Miyaji, T., Biswas, R., Li, T., Sano, H., Shi, Z., Takahashi, S., Tong, J., 2016. Effects of soil erosion and anoxic-euxinic ocean in the Permian-Triassic marine crisis. Heliyon 2, e00137.

Kershaw, S., 2015. Modern Black Sea oceanography applied to the end-Permian extinction event. Journal of Palaeogeography 4, 52–62.

Knoll, A.H., Bambach, R.K., Canfield, D.E., Grotzinger, J.P., 1996. Comparative Earth history and Late Permian mass extinction. Science 273, 452–457.

Knoll, A.H., Bambach, R.K., Payne, J.L., Pruss, S., Fischer, W.W., 2007. Paleophysiology and end-Permian mass extinction. Earth & Planetary Science Letters 256, 295–313.

Lehrmann, D.J., Payne, J.L., Felix, S.V., Dillett, P.M., Wang, H.M., Yu, Y.Y., Wei, J.Y., 2003. Permian-Triassic boundary sections from shallow-marine carbonate platforms of the Nanpanjiang Basin, South China: implications for oceanic conditions associated with the end-Permian extinction and its aftermath. Palaios 18, 138–152.

Lei, L.D., Shen, J., Li, C., Algeo, T.J., Chen, Z.Q., Feng, Q.L., Cheng, M., Jin, C.S., Huang, J.H., 2017. Controls on regional marine redox evolution during Permian-Triassic transition in South China. Palaeogeography, Palaeoclimatology, Palaeoecology 486, 17–32.

Li, G.S. Wang, Y.B., Shi, G.R., Liao, W., Yu, L.X., 2016. Fluctuations of redox conditions across the Permian-Triassic boundary-New evidence from the GSSP section in Meishan of South China. Palaeogeography, Palaeoclimatology, Palaeoecology 448, 48–58.

Liao, W., Bond, D.P.G., Wang, Y.B., He, L., Yang, H., Weng, Z.T., Li, G.S., 2017. An extensive anoxic event in the Triassic of the South China Block: A pyrite framboid study from Dajiang and its implications for the causes of oxygen depletion. Palaeogeography, Palaeoclimatology, Palaeoecology 486, 86–95.

Liao, W., Wang, Y.B., Kershaw, S., Weng, Z.T., Yang, H., 2010. Shallow-marine dysoxia across the Permian-Triassic boundary: Evidence from pyrite framboids in the microbialite in South China. Sedimentary Geology 232, 77-83.

Liu, S.A., Wu, H.C., Shen, S.Z., Jiang, G.Q., Zhang, S.H., Lv, Y.W., Zhang, H., Li, S.G., 2017. Zinc isotope evidence for intensive magmatism immediately before the end-Permian mass extinction. Geology 45, 343–346.

Loope, G.R., Kump, L.R., Arthur, M.A., 2013. Shallow water redox conditions from the Permian–Triassic boundary microbialite: The rare earth element and iodine geochemistry of carbonates from Turkey and South China. Chemical Geology 351, 195–208.

Meyer, K.M., Kump, L.R., 2008. Oceanic euxinia in Earth history: causes and consequences. Annual Review of Earth & Planetary Sciences 36, 251–288.

Newton, R., Bond, D., Cope, H., Wignall, P.B., 2009. A “framboidal gap” at the Permo-Triassic boundary. Goldschmidt Conference Abstracts, p. 939.

Nielsen, K.J., Shen, Y.A., 2004. Evidence for sulfidic deep water during the Late Permian in the East Greenland Basin. Geology 32 (12), 1037–1040.

Nielsen, K.J., Shen, Y.A., Piasecki, S., Stemmerik, L., 2010. No abrupt change in redox condition caused the end-Permian marine ecosystem collapse in the East Greenland Basin. Earth and Planetary Science Letters 291, 32–38.

Schubert, J.K., Bottjer, D.J., 1995. Aftermath of the Permian–Triassic mass extinction event: paleoecology of Lower Triassic carbonates in the western USA. Palaeogeography, Palaeoclimatology, Palaeoecology 116, 1–39.

Shen, J., Feng, Q.L., Algeo, T.J., Li, C., Planavsky, N.J., Zhou, L., Zhang, M.L., 2016. Two pulses of oceanic environmental disturbance during the Permian-Triassic boundary crisis. Earth and Planetary Science Letters 443, 139–152.

Shen, S., Crowley, J.L., Wang, Y., Bowring, S.A., Erwin, D.H., Sadler, P.M., Cao, C., Rothman, D.H., Henderson, C.M., Ramezani, J., 2011. Calibrating the end-Permian mass extinction. Science 334, 1367–1372.

Słowakiewicz, M., Tucker, M.E., Perri, E., Pancost, R.D., 2015. Nearshore euxinia in the photic zone of an ancient sea. Palaeogeography, Palaeoclimatology, Palaeoecology 426, 242–259.

Song, H.J., Wignall, P.B., Chu, D., Tong, J., Sun, Y., Song, H.Y., He, W., Tian, L., 2014. Anoxia/high temperature double whammy during the Permian-Triassic marine crisis and its aftermath. Scientific Reports 4, 4132.

Song, H.Y., Tong, J.N., Algeo, T.J., Horacek, M., Qiu, H.O., Song, H.J., Tian, L., Chen, Z.Q., 2013. Large vertical $\delta^{13}C_{DIC}$ gradients in Early Triassic seas of the South China craton: implications for oceanographic changes related to Siberian Traps volcanism. Global and Planetary Change 105, 7–20.

Tang, H., Kershaw, S., Liu, H., Tan, X.C., Li, F., Hu, G., Huang, C., Wang, L.C., Lian, C.B., Li, L., Yang, X.F., 2017. Permian-Triassic boundary microbialites (PTBMs) in southwest China: implications for paleoenvironment reconstruction. Facies 63(1), 2.

Takahashi, S., Yamasaki, S.-i., Ogawa, Y., Kimura, K., Kaiho, K., Yoshida, T., Tsuchiya, N., 2014. Earth and Planetary Science Letters 393, 94–104.

Tian, L., Tong, J.N., Algeo, T.J., Song, H.J., Chu, D.L., Shi, L., Bottjer, D.J., 2014. Reconstruction of Early Triassic ocean redox conditions based on framboidal pyrites from the Nanpanjiang Basin, South China. Palaeogeography, Palaeoclimatology, Palaeoecology 412, 68–79.

Tian, L., Tong, J.N., Bottjer, D., Chu, D., Liang, L., Song, H.J., Song, H.Y., 2015. Rapid carbonate depositional changes following the Permian-Triassic mass extinction: Sedimentary evidence from South China. Journal of Earth Science 26, 166–180.

Tian, L., Tong, J.N., Xiao, Y.F., Benton, M.J., Song, H.Y., Song, H.J., Liang, L., Wu, K., Chu, D.L., Algeo, T.J., 2018. Environmental instability prior to end-Permian mass extinction on shallow carbonate platforms of the Nanpanjiang Basin. Palaeogeography, Palaeoclimatology, Palaeoecology, in press; doi: 10.1016/j.palaeo.2018.05.011.

Twitchett, R.J., Krystyn, L., Baud, A., Wheeley, J.R., Richoz, S., 2004. Rapid marine recovery after the end-Permian mass-extinction event in the absence of marine anoxia. Geology 32, 805–808.

Wang, L., Wignall, P.B., Wang, Y., Jiang, H., Sun, Y., Li, G., Yuan, J., Lai, X., 2015. Depositional conditions and revised age of the Permo-Triassic microbialites at Gaohua section, Cili County (Hunan Province, South China). Palaeogeography, Palaeoclimatology, Palaeoecology 443, 156–166.

Wei, H., Shen, J., Schoepfer, S.D., Krystyn, L., Richoz, S., Algeo, T.J., 2015a. Environmental controls on marine ecosystem recovery following mass extinctions, with an example from the Early Triassic. Earth-Science Reviews 149, 108–135.

Wei, H., Algeo, T.J., Yu, H., Wang, J., Guo, C., Shi, G., 2015b. Episodic euxinia in the Changhsingian (late Permian) of South China: Evidence from framboidal pyrite and geochemical data. Sedimentary Geology 319, 78–97.

Wignall, P.B., Hallam, A., 1992. Anoxia as a cause of the Permian/Triassic extinction: facies evidence from northern Italy and the western United States. Palaeogeography Palaeoclimatology Palaeoecology 93, 21–46.

Wignall, P.B., Newton, R., 1998. Pyrite framboid diameter as a measure of oxygen deficiency in ancient mudrocks. American Journal of Science 298, 537–552.

Wignall, P.B., Twitchett, R.J., 1996. Oceanic anoxia and the end Permian mass extinction. Science 272, 1155–1158.

Wignall, P.B., Twitchett, R.J., 2002. Extent, duration, and nature of the Permian–Triassic superanoxic event. In: Koeberl, C., Macleod, K.G. (Eds.), Catastrophic events and mass extinctions: impacts and beyond. Geological Society of America Special Paper 356, 395–414.

Wignall, P.B., Newton, R., Brookfield, M.E., 2005. Pyrite framboidal evidence for oxygen-poor deposition during the Permian-Triassic crisis in Kashmir. Palaeogeography Palaeoclimatology Palaeoecology 216, 183–188.

Wignall, P.B., Bond, D.P.G., Kuwahara, K., Kakuwa, Y., Newton, R.J., Poulton, S.W., 2010. An 80 million year oceanic redox history from Permian to Jurassic pelagic sediments of the Mino–Tamba terrane, SW Japan, and the origin of four mass extinctions. Global and Planetary Change 71, 109–123.

Wignall, P.B., Bond, D.P.G., Sun, Y.D., Grasby, S.E., Beauchamp, B., Joachimski, M.M., Blomeier, D.P.G., 2016. Ultra-shallow-marine anoxia in an Early Triassic shallow-marine clastic ramp (Spitsbergen) and the suppression of benthic radiation. Geological Magazine 153, 316–331.

Wilkin, R.T., Barnes, H.L., Brantley, S.L., 1996. The size distribution of framboidal pyrite in modern sediments: an indicator of redox conditions. Geochimica Cosmochimica Acta 60, 3897–3912.

Xie, S., Pancost, R.D., Wang, Y., Yang, H., Wignall, P.B., Luo, G., Jia, C., Chen, L., 2010. Cyanobacterial blooms tied to volcanism during the 5 my Permo-Triassic biotic crisis. Geology 38, 447–450.

Yin, H., Jiang, H., Xia, W., Feng, Q., Zhang, N., Shen, J., 2014. The end-Permian regression in South China and its implication on mass extinction. Earth-Science Reviews 137, 19–33.

Zhang, G.J., Zhang, X.L., Hu, D.P., Li, D.N., Algeo, T.J., Farquhar, J., Henderson, C.M., Qin, L.P., Shen, M, Shen, D., Schoepfer, S.D., Chen, K.F., Shen, Y.A., 2017. Redox chemistry changes in the Panthalassic Ocean linked to the end-Permian mass extinction and delayed Early Triassic biotic recovery. Proceedings of the National Academy of Sciences, USA 114, 1806–1810.

Zhang, R., Follows, M.J., Grotzinger, J.P., Marshall, J., 2001. Could the Late Permian deep ocean have been anoxic? Paleoceanography 16, 317–329.

Zhao, X.M., Tong, J.N., 2010. Two episodic changes of trace fossils through the Permian–Triassic transition in the Meishan cores, Zhejiang Province. *Science China Earth Sciences* 53, 1885–1893.

Zheng, Q.F., Cao, C.Q., Zhang, M.Y., 2013. Sedimentary features of the Permian–Triassic boundary sequence of the Meishan section in Changxing County, Zhejiang Province. Science China Earth Sciences 56, 956–969.

Zhou, W., Algeo, T.J., Ruan, X., Luo, G., Chen, Z.Q., Xie, S., 2017. Expansion of photic-zone euxinia during the Permian-Triassic biotic crisis and its causes: Microbial biomarker records. Palaeogeography Palaeoclimatology Palaeoecology 474, 140–151.

Figure Captions

Fig. 1. Palaeogeography of (A) the world and (B) the Nanpanjiang Basin of the South China Craton during the Permian-Triassic transition. Map B shows the study section location (red) on the isolated carbonate platform (blue): TP = Taiping. The South China Block has rotated nearly 90° clockwise since the Permian-Triassic. Map A is adapted from Ron Blakey (http://jan.ucc.nau.edu/rcb7/), while map B is modified after Lehrmann et al. (2003) and Algeo et al. (2007).

Fig. 2. Outcrop photos of the Taiping section. (A) Uppermost Heshan and lowermost Majiaoling formations (the Permian-Triassic boundary is associated with the formation contact; red line). (B) Truncation surface (red arrow) between uppermost Permian bioclastic limestones and lowermost Triassic microbialites, and a stylolite located 2 cm above (blue arrow). (C) Thrombolitic microbialites of the basal Majiaoling Formation (ruler = 10 cm).

Fig. 3. Thin section microscopic photos of the bioclastic limestone and sandy limestone from uppermost Heshan Formation. (A) and (B) bioclastic packstone with diverse skeletons, indicating open marine platform environment; (C) packstone with foraminifers and sponge spicules, implying relative deeper environment; (D) sandy mudstone with numerous detrital minerals (e.g. quartzes).

Fig. 4. Thin section microscopic photos of the lowermost Majiaoling microbialites. (A) tiny radial carbonate fan precipitates and foraminifer *Globivalvulina bulloides*; (B) ostracods are enriched in the micritic clots; two different calcified possible cyanobacteria: (C) cluster of coccoidal micritic clots, and (D) lunate chambered micritic belts, interpreted as *Renalcis*-like microbe.

Fig. 5. SEM photos of conodonts from the Taiping section. Note that all specimens are from the lowermost Majiaoling microbialites. A–D: *Hindeodus parvus*, A, specimen TP112, B, TP111, C, specimen TP116, D, specimen TP110; E and I–L: *Hindeodus praeparvus*, E, specimen TP121, I, specimen TP115, J, specimen TP117, K, specimen TP109, L, specimen TP119; F: *Hindeodus eurypyge*, specimen TP120; G: *Hindeodus changxingensis*, specimen TP114; H: *Hindeodus inflatus*, specimen TP113.

Fig. 6. Integrated diagram of microfacies changes, conodont distribution, and carbon isotope and framboid size distributions. Details of statistical indexes for framboid size distribution of each sample are presented in Table 1. MFT = Microfacies types: MF1, foraminiferal packstone; MF2, algal-foraminiferal packstone; MF3, sandy mudstone; MF4, dolomitized wackestone. Raw data of carbon, S_{pyrite} isotopes and content of S_{pyrite} are in online supporting material Table S1.

Fig. 7. SEM photos of pyrite specimens from the Taiping section. A, small framboidal pyrite (diam. < 6 μm), sample TP-12, photo (042); B, pyrite cluster, mixture of euhedral and framboidal pyrites, sample TP-13, photo (082); C–D, small and large (diam. > 10 μm) framboids, C, sample TP-10, photo (028), D, sample TP-1, photo (075); E–F, mixture of euhedral pyrites with framboids, sample TP-7, E, photo (006), F, photo (056).

Fig. 8. MSD diagram for redox condition reconstruction. Mean size versus standard deviation of framboidal pyrites. Euxinic samples are separated from the dysoxic samples by the dotted line, which is from Wilkin et al. (1996). Numbered circles stand for the corresponding samples in Table S2.

Fig. 9. $\delta^{34}S_{pyrite}$ versus Pyrite S content. The dashed line A shows the potential terrestrial-input controlled fraction while the solid line B shows the syngenetic and authigenic pyrite mixed fraction (from Algeo et al. 2008). Raw data of S_{pyrite} isotopes and content of S_{pyrite} are in online supporting material Table S1.

Fig. 10. Comprehensive diagram of temporal biotic and redox conditional changes. Fossil frequency and distribution of foraminifera are from Tian et al. (2018), while the distributions of conodonts and redox conditions are simplified from Fig. 6 of this study. The solid line for the redox reconstruction (right-hand side) is based on the mean values of the studied samples.

Fig. 11. Global comparison diagram of the framboidal pyrites based redox histories in different facies and sections during Permian-Triassic transition. The studied sections are organized by lithological compositions (facies): (1) shallow marine carbonate successions (shallow platforms and margin sections) are listed in the uppermost row; (2) mudstone and claystone interbedded carbonate successions (slope sections) are listed in the middle row; (3) mudstone and chert dominated deep water successions (basinal sections) are listed in the lowermost row. Note: EPME = end-Permian mass extinct. Data sources: Taiping from this study; Dajiang from Liao et al. (2017); Laolongdong from Liao et al. (2010); Cili from Wang et al. (2015); Bulla, Balvany North, Shangsi, Tianqiao and Hovea from Bond and Wignall (2010); Chaotian from Newton et al. (2009); Meishan from Li et al. (2016); Xiaojiaba from Wei et al. (2015b); Changtanhe from He et al. (2013); Xiakou from Shen et al. (2016); Guryul Ravine from Wignall et al. (2005); Fiskegrav from Nielson et al. (2010); Ubara from Algeo et al. (2011); Tschermakfjellet from Dustira et al. (2013).

Highlights

- Pyrite framboid size distributions and $\delta^{34}S_{pyrite}$ suggest low oxygen levels throughout the EPME in the Taiping section;
- Shallow marine euxinia occurred prior to the EPME on the Pingguo Platform;
- Large-sized framboidal pyrites in the basal Permian-Triassic microbialite indicate an earliest Triassic oxygenation event;
- A potential terrestrial input controlled fraction dynamic of $\delta^{34}S_{pyrite}$ was proposed to interpret the pre-EPME heavy $\delta^{34}S_{pyrite}$;
- Shallow dysoxia of the Nanpangjiang Basin might have invaded from intra shelf basins rather than the Panthalassic Ocean.

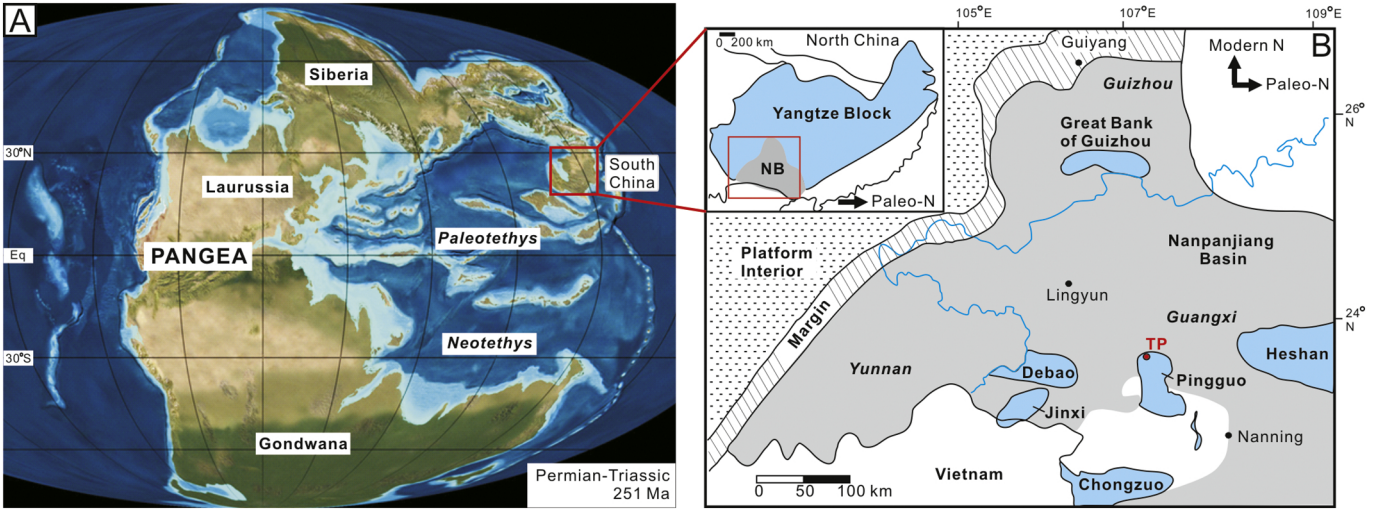
A
Siberia
30°N
Laurussia
South China
Eq
PANGEA
Paleotethys
30°S
Neotethys
Gondwana
Permian-Triassic
251 Ma
105°E
107°E
109°E
0 200 km
North China
Yangtze Block
NB
Paleo-N
Guiyang
Modern N
B
Paleo-N
Guizhou
26° N
Great Bank of Guizhou
Nanpanjiang Basin
Platform Interior
Margin
Lingyun
Guangxi
24° N
TP
Heshan
Yunnan
Debao
Pingguo
Jinxi
Nanning
Vietnam
Chongzuo
0 50 100 km

Figure 1


A
Majiaoling Formation
Heshan Formation
B
microbialites
bioclastic
limestone
C

Figure 2

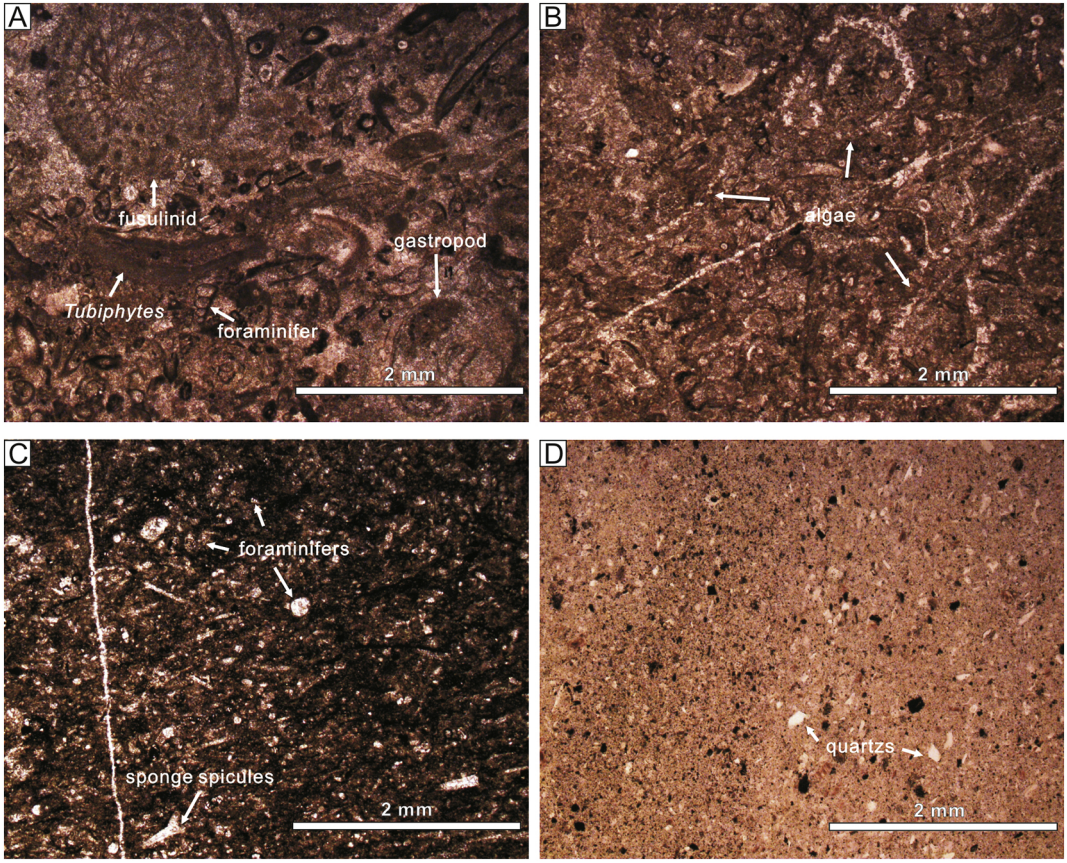
A
fusulinid
gastropod
Tubiphytes
foraminifer
2 mm
B
algae
2 mm
C
foraminifers
sponge spicules
2 mm
D
quartzs
2 mm

Figure 3

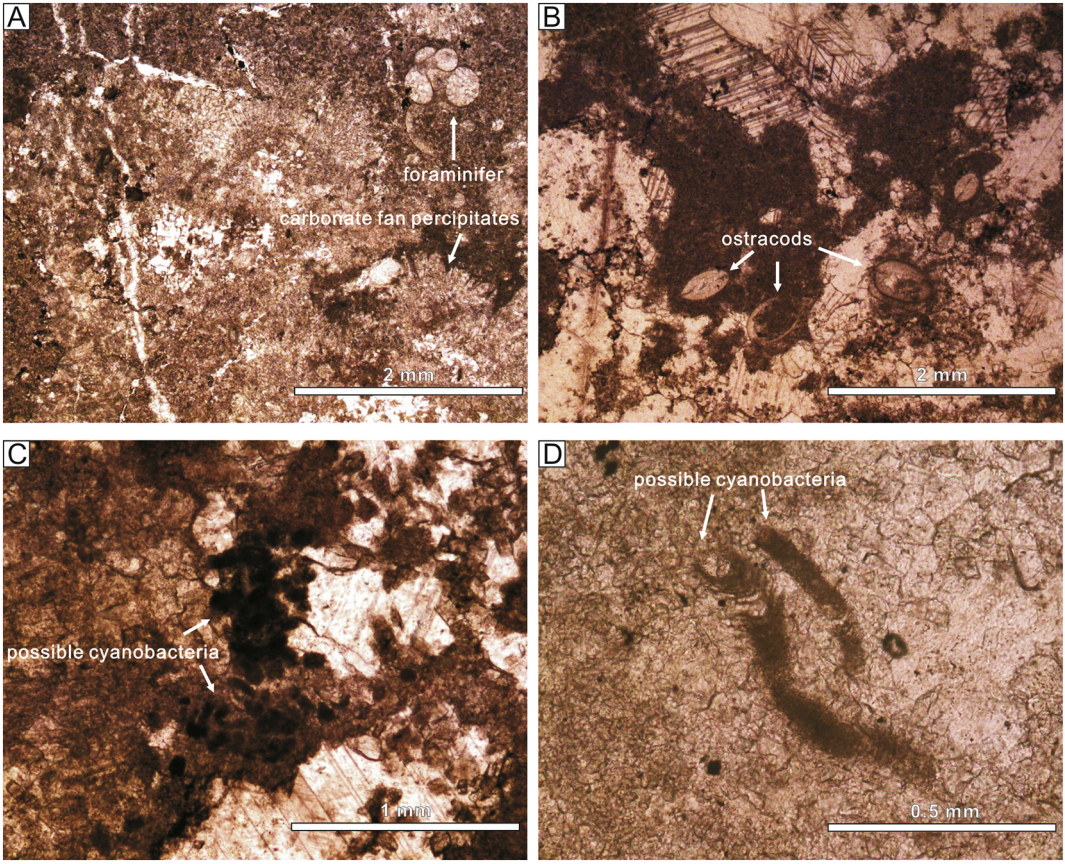
A
foraminifer
carbonate fan percipitates
2 mm
B
ostracods
2 mm
C
possible cyanobacteria
1 mm
D
possible cyanobacteria
0.5 mm

Figure 4

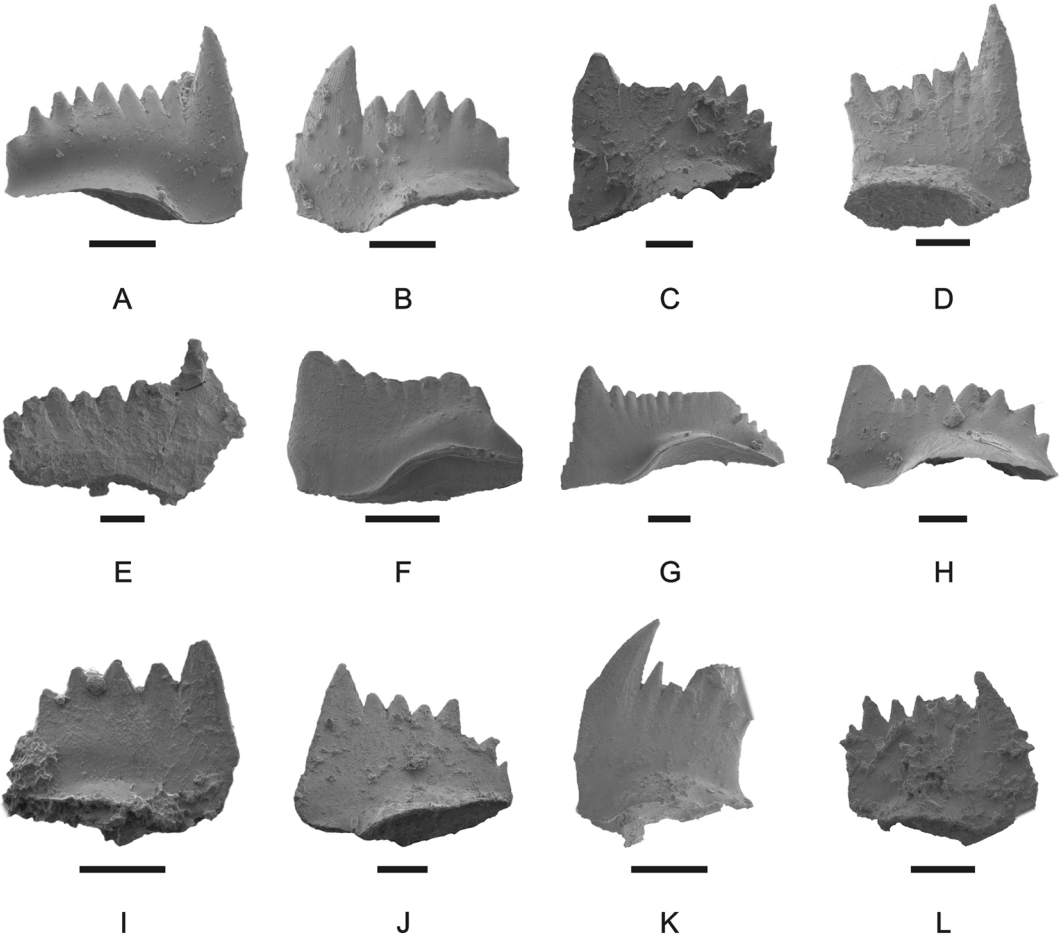

Figure 5

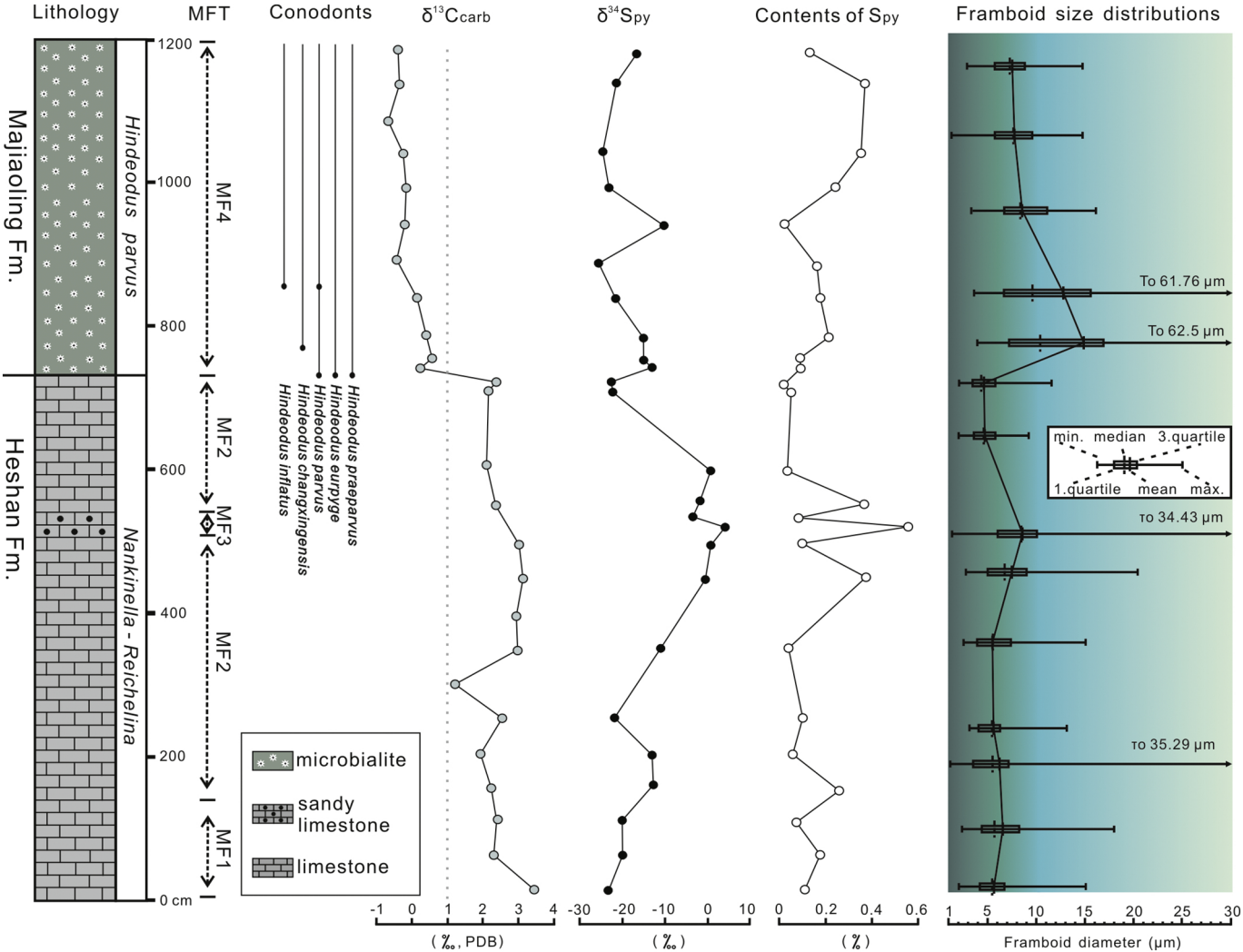
Lithology
MFT
Conodonts
δ13Ccarb
δ34Spy
Contents of Spy
Framboid size distributions
Majiaoling Fm.
Heshan Fm.
Hindeodus parvus
Nankinella - Reichelina
MF4
MF2
MF3
MF2
MF1
1200
1000
800
600
400
200
0 cm
Hindeodus praeparvus
Hindeodus eurpyge
Hindeodus parvus
Hindeodus changxingensis
Hindeodus inflatus
microbialite
sandy limestone
limestone
-1 0 1 2 3 4
(‰, PDB)
-30 -20 -10 0 10
(‰)
0 0.2 0.4 0.6
(%)
To 61.76 μm
To 62.5 μm
min. median 3.quartile
1.quartile mean max.
то 34.43 μm
то 35.29 μm
1 5 10 15 20 25 30
Framboid diameter (μm)

Figure 6

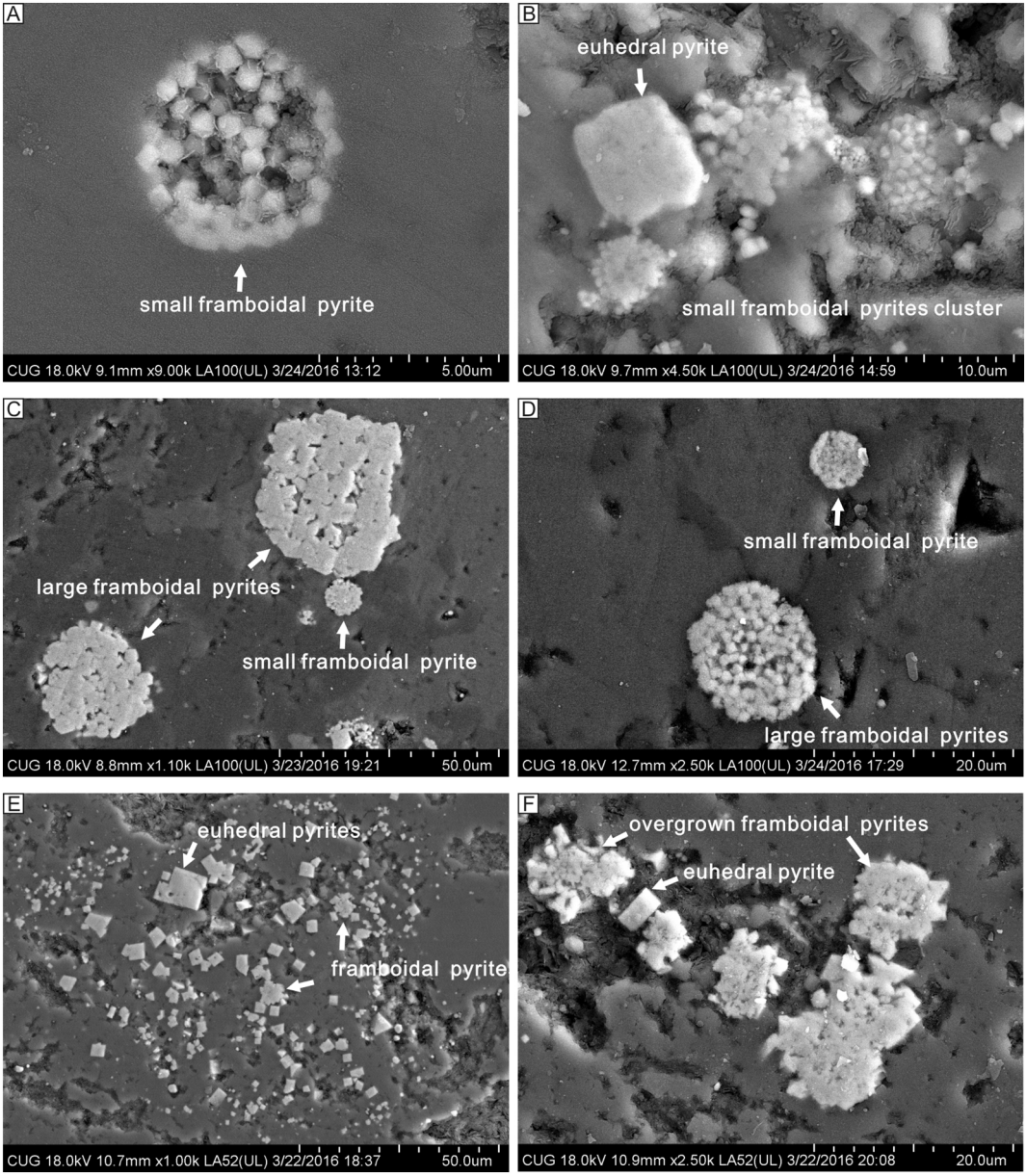
A
small framboidal pyrite
CUG 18.0kV 9.1mm x9.00k LA100(UL) 3/24/2016 13:12 5.00um
B
euhedral pyrite
small framboidal pyrites cluster
CUG 18.0kV 9.7mm x4.50k LA100(UL) 3/24/2016 14:59 10.0um
C
large framboidal pyrites
small framboidal pyrite
CUG 18.0kV 8.8mm x1.10k LA100(UL) 3/23/2016 19:21 50.0um
D
small framboidal pyrite
large framboidal pyrites
CUG 18.0kV 12.7mm x2.50k LA100(UL) 3/24/2016 17:29 20.0um
E
euhedral pyrites
framboidal pyrite
CUG 18.0kV 10.7mm x1.00k LA52(UL) 3/22/2016 18:37 50.0um
F
overgrown framboidal pyrites
euhedral pyrite
CUG 18.0kV 10.9mm x2.50k LA52(UL) 3/22/2016 20:08 20.0um

Figure 7

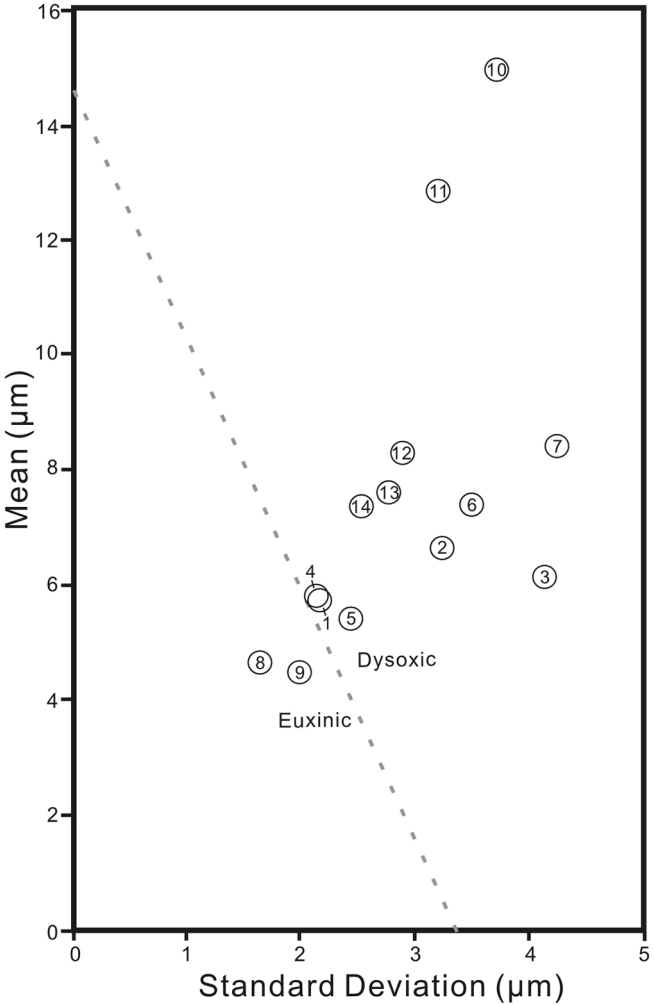
Mean (μm)
Standard Deviation (μm)
Dysoxic
Euxinic
0
1
2
3
4
5
6
7
8
9
10
11
12
13
14
0
2
4
6
8
10
12
14
16

Figure 8

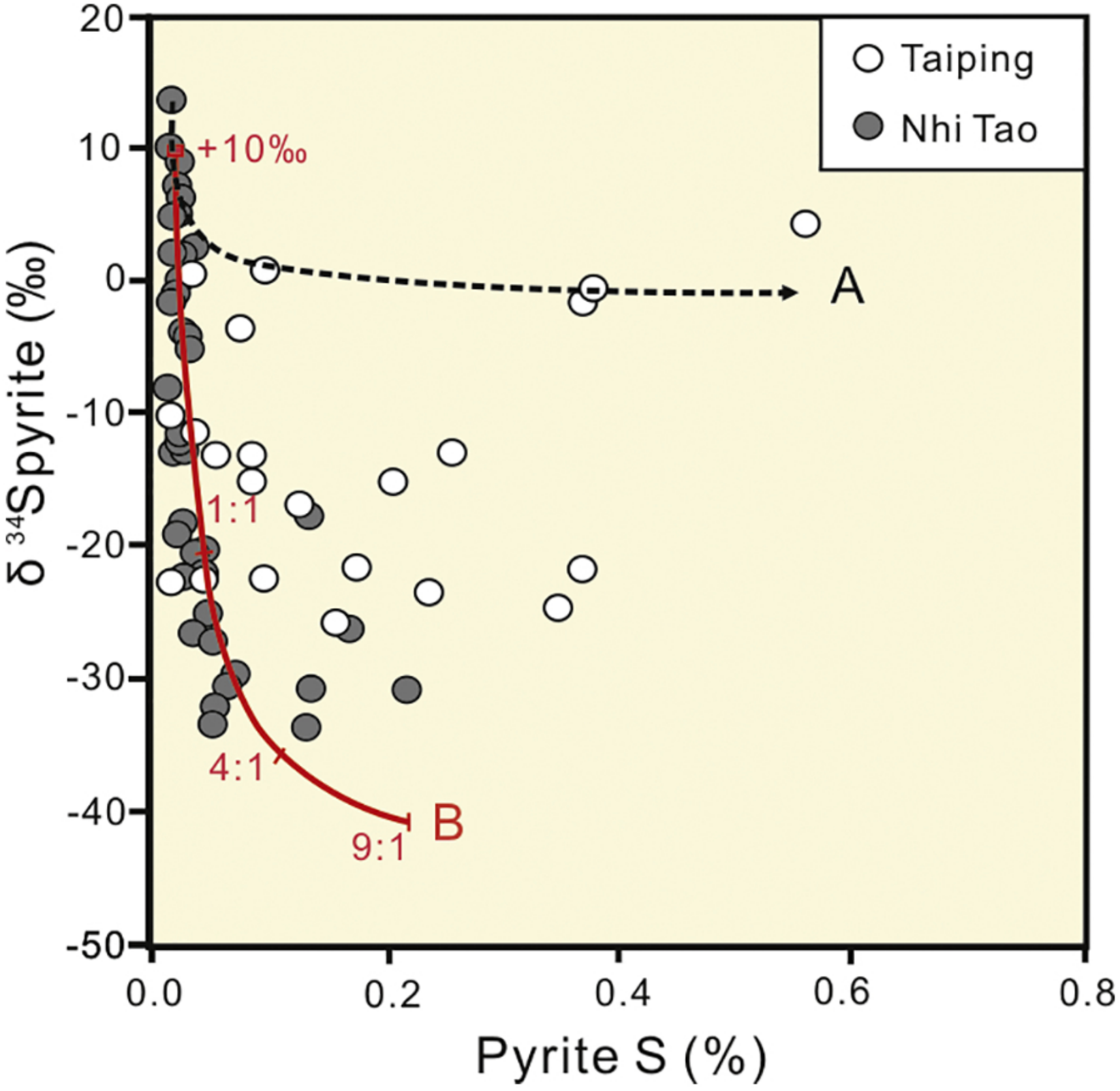
Taiping
Nhi Tao
+10‰
A
1:1
4:1
9:1
B
δ 34Spyrite (‰)
Pyrite S (%)
20
10
0
-10
-20
-30
-40
-50
0.0
0.2
0.4
0.6
0.8

Figure 9

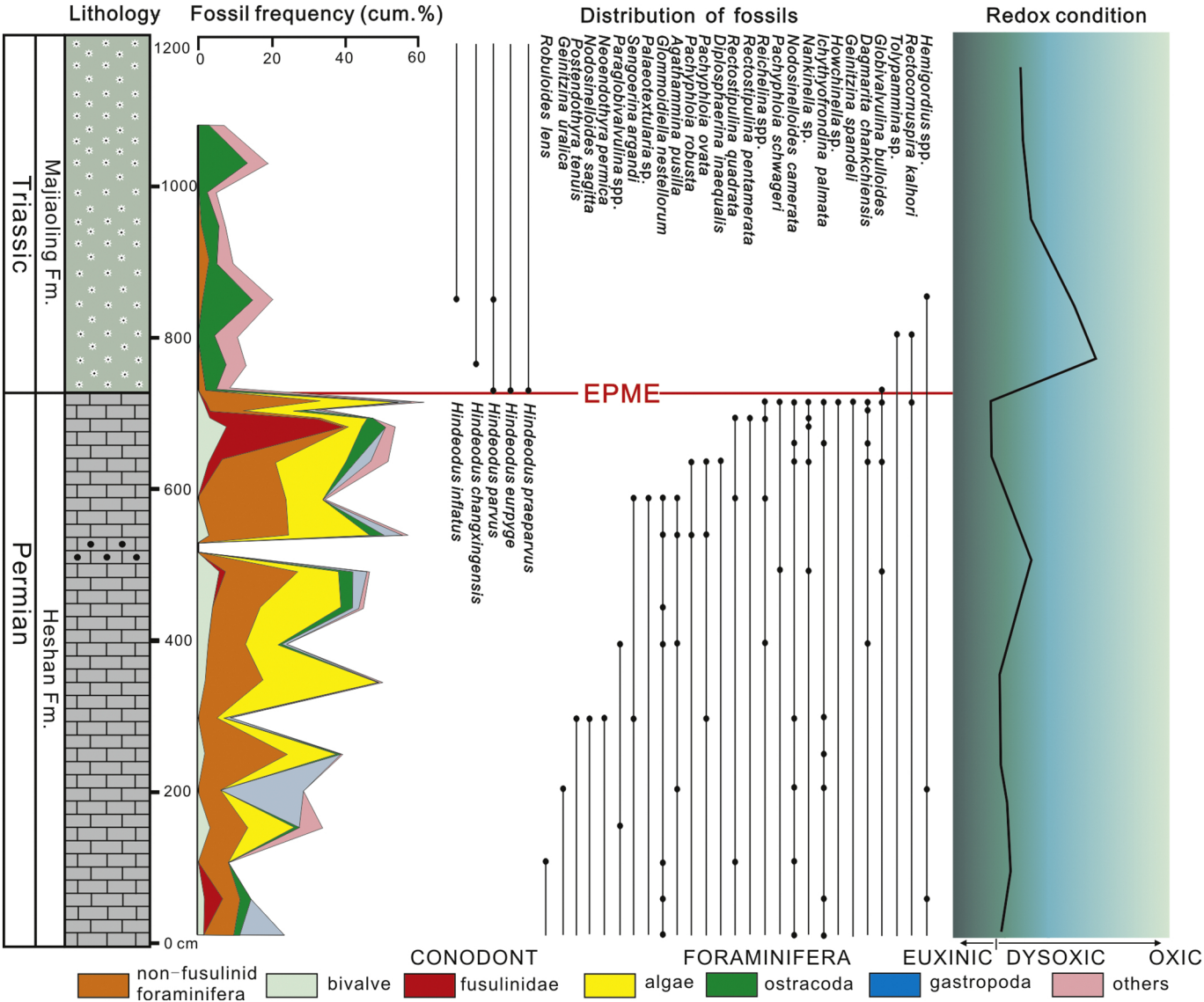
Lithology
Fossil frequency (cum.%)
Distribution of fossils
Redox condition
Triassic
Permian
Majiaoling Fm.
Heshan Fm.
1200
1000
800
600
400
200
0 cm
0
20
40
60
Hemigordius spp.
Rectocornuspira kalhori
Tolypammina sp.
Globivalvulina bulloides
Dagmarita chankchiensis
Geinitzina spandeli
Howchinella sp.
Ichthyofrondina palmata
Nankinella sp.
Nodosinelloides camerata
Pachyphloia schwageri
Reichelina spp.
Rectostipulina pentamerata
Rectostipulina quadrata
Diplosphaerina inaequalis
Pachyphloia ovata
Pachyphloia robusta
Agathammina pusilla
Glommoidiella nestellorum
Palaeotextularia sp.
Sengoerina argandi
Paraglobivalvulina spp.
Neoendothyra permica
Nodosinelloides sagitta
Postendothyra tenuis
Geinitzina uralica
Robuloides lens
Hindeodus praeparvus
Hindeodus eurpyge
Hindeodus parvus
Hindeodus changxingensis
Hindeodus inflatus
EPME
EUXINIC
DYSOXIC
OXIC
CONODONT
FORAMINIFERA
non-fusulinid foraminifera
bivalve
fusulinidae
algae
ostracoda
gastropoda
others

Figure 10

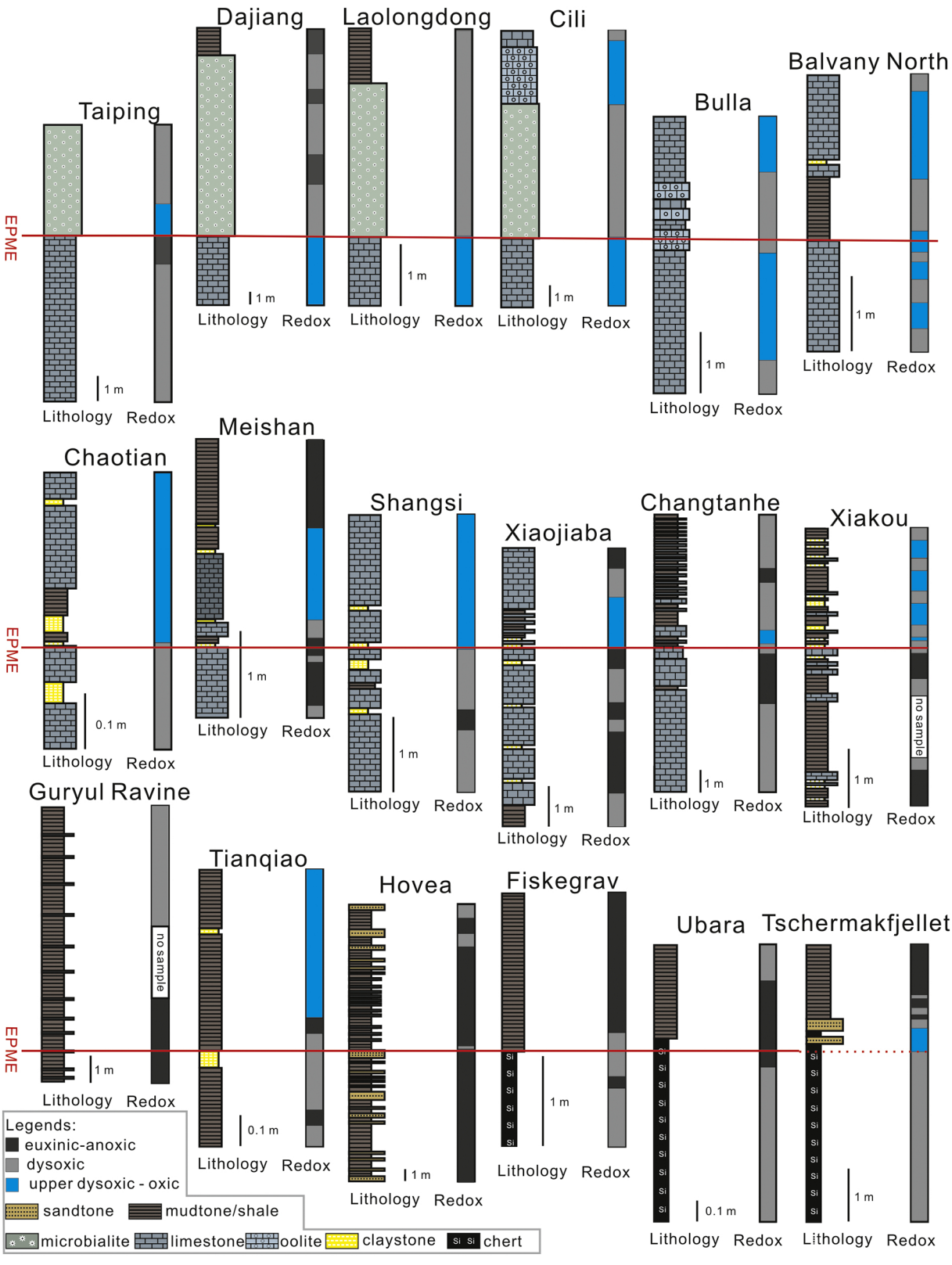
Taiping
Dajiang
Laolongdong
Cili
Bulla
Balvany North
Chaotian
Meishan
Shangsi
Xiaojiaba
Changtanhe
Xiakou
Guryul Ravine
Tianqiao
Hovea
Fiskegrav
Ubara
Tschermakfjellet
EPME
1 m
0.1 m
Lithology
Redox
no sample
Si
Legends:
euxinic-anoxic
dysoxic
upper dysoxic - oxic
sandtone
mudtone/shale
microbialite
limestone
oolite
claystone
chert

Figure 11